Scilight

International Journal of Gravitation and Theoretical Physics
https://www.sciltp.com/journals/ijgtp

Article

Check for updates

Observational Signatures of Misaligned Double-Ring and Double-Torus Configurations around a Schwarzschild Black Hole

Dmitriy Ovchinnikov [*,†], Jan Schee [†] and Zdeněk Stuchlík [†]

Research Centre for Theoretical Physics and Astrophysics, Institute of Physics, Silesian University in Opava, Bezručovo nám. 13, Opava 746 01, Czech Republic
* Correspondence: dmitriy.ovchinnikov@physics.slu.cz
† These authors contributed equally to this work.

How To Cite: Ovchinnikov, D.; Schee, J.; Stuchlík, Z. Observational Signatures of Misaligned Double-Ring and Double-Torus Configurations around a Schwarzschild Black Hole. *International Journal of Gravitation and Theoretical Physics* **2026**, *2*(2), 7. https://doi.org/10.53941/ijgtp.2026.200007

Received: 13 May 2026
Revised: 5 June 2026
Accepted: 8 June 2026
Published: 30 June 2026

Abstract: We investigate the observational signatures of an idealized double-ring and double-torus system orbiting a Schwarzschild black hole, allowing the two emitting components to have mutually inclined symmetry axes. Using general-relativistic ray tracing, we construct frequency-shift maps, bolometric flux maps on the observer's screen, and the corresponding spectral line profiles of the emitted radiation. The single equatorial torus is used as a reference configuration in order to isolate the effect of the second emitting component and of the mutual misalignment of the two structures. We show that the presence of two non-coplanar emitting structures produces characteristic multi-peak spectral profiles and asymmetric bolometric-flux distributions. These signatures are imprinted both in the line-profile morphology and in the α-profiles of the bolometric flux, providing simple diagnostic features of non-coplanar multi-component accretion structures.

Keywords: Schwarzschild black hole; misaligned tori; double-ring emission

1. Introduction

Recent progress in very-long-baseline interferometry has opened a direct observational window onto the horizon-scale environment of supermassive black holes. The Event Horizon Telescope (EHT) observations of M87* and Sgr A* have revealed compact, asymmetric emission regions shaped by strong gravitational lensing, relativistic plasma motion, and radiative processes in the immediate vicinity of the central object [1,2]. These observations are commonly interpreted with the aid of general-relativistic magnetohydrodynamical (GRMHD) simulations combined with general-relativistic radiative transfer and ray-tracing techniques [3–5]. Such simulations provide the most realistic description of black-hole accretion flows currently available. At the same time, simplified semi-analytical models remain useful, because they isolate individual geometrical and relativistic effects and allow one to identify which features of images and spectra are caused by a small number of physical parameters.

Accretion onto compact objects is one of the main mechanisms responsible for strong X-ray emission from black-hole systems [6–8]. The observed radiation carries information about the geometry, motion, and optical properties of the emitting plasma, since relativistic Doppler shifts, gravitational redshift, light bending, and focusing strongly modify the observed spectra and line profiles [9–11]. In many theoretical models the emitting matter is represented either by geometrically thin disks [6,7], by narrow radiating rings [12,13], or by geometrically thick, pressure-supported tori [14–16]. In particular, thick tori provide a useful idealization of non-spherical accretion structures and have been widely used to study relativistic images, radiation fluxes, and spectral line profiles in the strong-field region of black holes [15,17].

A further motivation for considering multi-component emitting structures comes from the theory of ringed accretion disks. In this framework, the accretion environment may consist of several pressure-supported tori or ring-like structures orbiting the same central black hole [18,19]. Such configurations can be interpreted as idealized stages of

a more complicated accretion history, for example when matter with different angular momentum is supplied to the central region. The dynamical evolution of interacting double-torus systems has also been studied numerically, showing that such systems are generally not expected to remain permanently isolated and may undergo interaction, accretion, or merging phases [20].

The possibility of non-coplanar accretion structures is motivated by a broader class of tilted, warped, or broken accretion flows. Misaligned accretion disks can arise when the angular-momentum axis of the inflowing matter does not coincide with a preferred symmetry axis of the system. Numerical simulations of tilted accretion flows have shown that their images and spectral line profiles can differ substantially from those of aligned disks and may depend strongly on the observer's azimuthal position [21]. In addition, disk tearing mechanisms can produce several distinct ring-like components with different orbital planes [22,23]. Although such effects are often discussed in connection with rotating black holes, the Schwarzschild spacetime provides a clean reference case in which the influence of the source geometry can be studied without frame dragging.

Misaligned aggregates of pressure-supported tori around static Schwarzschild black holes have recently been investigated from the point of view of hydrodynamical constraints, possible collisions, limiting configurations, energetics, and stability properties [24,25]. These studies motivate the question addressed here from a complementary point of view: how would a simplified non-coplanar double structure appear to a distant observer?

In the present work we study the ray-traced observational signatures of an idealized double-ring and double-torus system in Schwarzschild spacetime. The two emitting components are allowed to have mutually inclined symmetry axes. We do not assume that such a configuration represents a permanently stable global equilibrium. Rather, it is treated as a stationary radiative snapshot of a possible transient or quasi-stationary stage of a multi-component accretion flow. For this system we compute frequency-shift maps, bolometric flux maps on the observer's screen, α-profiles of the bolometric flux, and spectral line profiles. By comparing the non-coplanar double configurations with the corresponding single-torus and coplanar cases, we identify characteristic signatures produced by the presence of a second inclined emitting component.

2. Model

We consider two idealized models of radiating structures orbiting a Schwarzschild black hole. The first model consists of two narrow Keplerian rings and is used to study the formation of spectral line profiles in a simple multi-component source. The second model replaces the rings by finite-thickness pressure-supported tori and is used to construct bolometric flux maps and the corresponding one-dimensional flux profiles on the observer's screen. Throughout the paper we use geometrized units $G = c = M = 1$. The details of the null geodesic equations, the observer's impact parameters, the rotated coordinate frame, and the redshift calculation are summarized in Appendix A.

2.1. Rings

A radiating ring is modeled as a narrow circular distribution of test particles moving along Keplerian circular geodesics. The ring radius is restricted to the region outside the innermost stable circular orbit, $r_{\rm ISCO} = 6M$. The corresponding Keplerian angular velocity is

$$\Omega_K = \frac{1}{r^{3/2}}. \tag{1}$$

The local emitted specific intensity is modeled by a Gaussian line profile,

$$I_e(\nu_e) = I_0(r) \exp\left[-\frac{(\nu_e - \nu_0)^2}{\sigma^2}\right] \tag{2}$$

where ν_e is the emitted frequency, ν_0 is the rest-frame line frequency, and σ determines the intrinsic width of the emitted line. The radial dependence of the emissivity normalization $I_0(r)$ is specified for the radii used in the simulations in Table 1.

The double-ring system consists of an inner ring A and an outer ring B, as shown schematically in Figure 1. Because the Schwarzschild spacetime is spherically symmetric, each ring can be assigned its own orbital plane. The orientation of each ring is specified by the normal vector to its orbital plane. In general, the normal vectors $\vec{n}_A$ and $\vec{n}_B$ are not parallel, and the angle between them defines the mutual misalignment of the two rings. A schematic representation of this configuration is shown in Figure 1.

Table 1. Values of the emissivity normalization $I_0(r)$ used for the ring simulations.

r	I_0
6	1.00
8	0.02
10	0.01

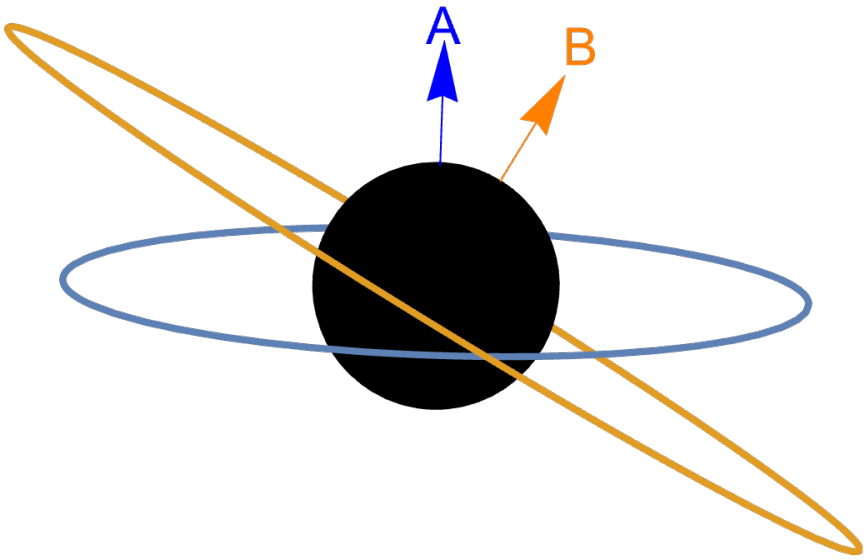

Figure 1. Schematic representation of the double-ring radiating structure. The rings A and B may have mutually inclined orbital planes.

The null geodesics connecting the emitting ring to the observer are obtained from the separated geodesic equations in Schwarzschild spacetime. Each geodesic is uniquely characterized by the impact parameters l and q, which are related to the observer's screen coordinates (α, β). In the ring calculations we include the primary-image contributions specified in Appendix A.1. The observed specific flux profile of a narrow ring is then written as

$$F(\nu_o; r_e) = \Delta r_e \int_{g_{\min}}^{g_{\max}} g^3 I_e(\nu_o/g; r_e) \left| \frac{\partial(\alpha, \beta)}{\partial(r_e, g)} \right| \mathrm{d}g, \tag{3}$$

where $g = \nu_o/\nu_e$ is the frequency-shift factor. The factor g^3 follows from the invariance of I_ν/ν^3, while the Jacobian of the mapping $(\alpha, \beta) \to (r_e, g)$ is evaluated numerically, as described in Appendix A.2.

2.2. Tori

We next consider finite-thickness radiating structures. Each torus is modeled as a stationary, axisymmetric, pressure-supported perfect-fluid configuration in Schwarzschild spacetime. The model corresponds to the standard Polish-doughnut construction with constant specific angular momentum l_{disk}. For such a configuration the equipressure and equidensity surfaces coincide with the equipotential surfaces [15]

$$W_0 = W(r, \theta') = \frac{1}{2} \ln \frac{(r - 2M) r^2 \sin^2 \theta'}{r^3 \sin^2 \theta' - (r^2 - 2M) l_{\mathrm{disk}}^2}. \tag{4}$$

Here θ' is the polar angle measured in the coordinate frame adapted to the symmetry axis of the corresponding torus. For an equatorial torus, $\theta' = \theta$. For an inclined torus, the relation between (r, θ, ϕ) and (r', θ', ϕ') is obtained by a rotation of the source-adapted frame about the original y-axis; the explicit transformation is given in Appendix A.3. The double-torus configuration is obtained by combining two such equipotential surfaces with different radial extensions and, in general, different symmetry axes. Representative meridional cross-sections of this geometry, viewed at different azimuthal angles, are shown in Figure 2.

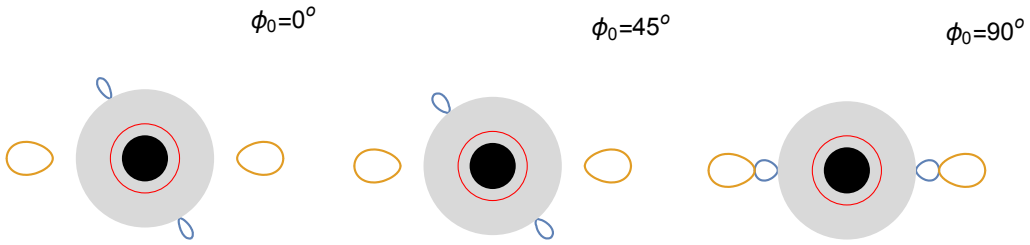

Figure 2. Meridional cross-sections of a double-torus structure viewed at three representative azimuthal angles $\phi_o = 0°, 45°, 90°$. The yellow and blue contours denote the outer edges of the two tori. The shaded region corresponds to the sphere $r_{\rm ISCO} = 6M$, the red circle marks the photon sphere $r_{\rm ph} = 3M$, and the black disk represents the black-hole horizon at $r_h = 2M$.

For the i-th torus we denote by $v^\mu_{(i)}$ the spacelike unit vector along its symmetry axis. The inclination angle $\theta_{(i)}$ between this axis and the normal n^μ to the original equatorial plane is defined by

$$\cos\theta_{(i)} = n_\mu v^\mu_{(i)}. \tag{5}$$

This definition allows us to distinguish between configurations with parallel toroidal symmetry axes and configurations in which the axes are mutually inclined. Examples of both cases are shown in Figure 3. Thus, each torus has its own source-adapted polar coordinate $\theta'_{(i)}$, which enters the potential $W(r, \theta'_{(i)})$. The explicit coordinate transformation and the transformation of the photon wave vector are not repeated here; they are given in Appendix A.3.

The ray-tracing procedure is performed backward from the observer's image plane. For each point (α, β) we integrate the corresponding null geodesic and search for intersections with the surfaces of both tori, defined by $W(r, \theta'_{(i)}) = W_{0(i)}$. If the ray intersects both surfaces, the first intersection along the backward ray is used. This prescription accounts for the geometrical occultation of the more distant emitting surface by the closer one, but it does not include absorption or scattering inside the toroidal matter.

At the emission point the observed-to-emitted frequency ratio is computed from

$$g = \frac{\nu_o}{\nu_e} = \frac{(k_\mu u^\mu)_o}{(k_\mu u^\mu)_e}.$$

For a circularly rotating perfect-fluid torus this gives the redshift formula stated in Appendix A.5. The angular velocity of the fluid is determined by $l_{\rm disk}$, and the photon angular momentum entering the redshift expression is evaluated in the rotated source-adapted frame.

The bolometric flux maps and spectral line profiles are then constructed using Liouville's theorem. The bolometric intensity transforms as $I_o = g^4 I_e$, while the specific intensity transforms as $I_{\nu_o} = g^3 I_{\nu_e}$. In the line-profile calculations we use a Gaussian local emissivity in the emitter frame. The explicit formulae used for the bolometric flux map and the spectral line profile are collected in Appendix A.6.

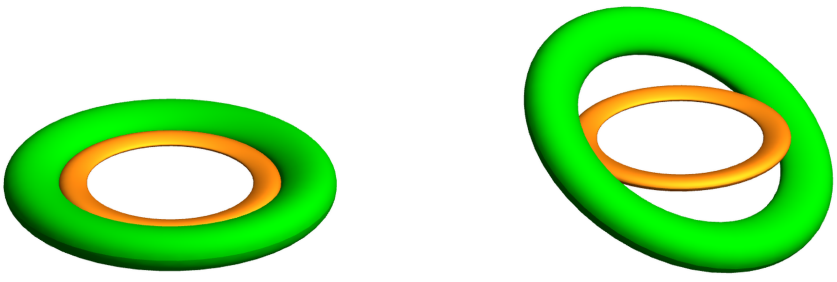

Figure 3. Three-dimensional visualization of two toroidal structures. The **left panel** shows a configuration with parallel symmetry axes, while the **right panel** shows a configuration with mutually inclined symmetry axes.

3. Results

We present the results in two steps. First, we analyze an idealized double-ring system. This simplified model allows us to isolate how the presence of two emitting radii and two different orbital planes affects the spectral line profile. Second, we consider finite-thickness double-torus configurations and study their bolometric flux maps and one-dimensional α-profiles on the observer's screen. For compactness, we denote the inclination angles of the inner and outer components by $\theta_A \equiv \theta_{i(A)}$ and $\theta_B \equiv \theta_{i(B)}$, respectively.

3.1. Double-Ring System

For the double-ring configurations we keep the inner ring A fixed at $(R_A, \theta_A) = (6M, 0°)$. The outer ring B is then varied in the parameter range

$$(R_B, \theta_B) \in [8M, 20M] \times [0°, 45°].$$

The observed line profile of the full system is a superposition of the individual contributions from rings A and B. An illustrative example is shown in Figure 4, where the combined profile is compared with the separate profiles of the two rings.

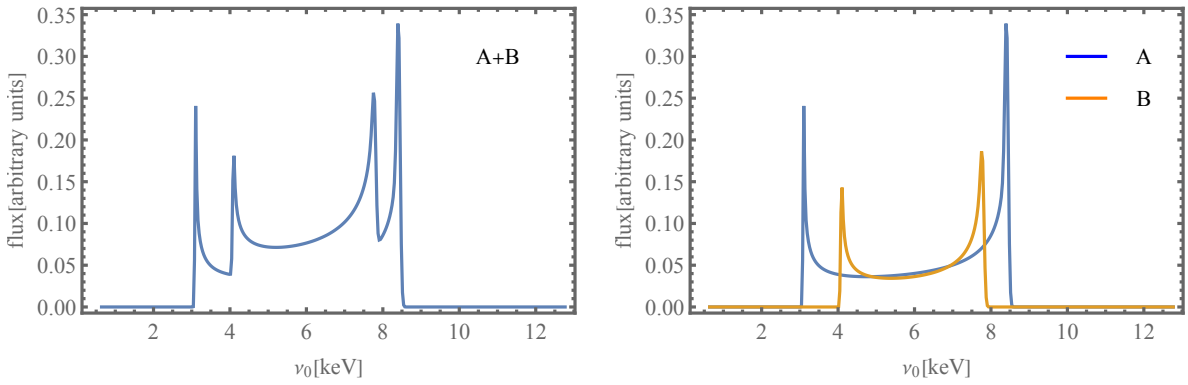

Figure 4. (**Left**): spectral line profile of the combined double-ring system $A + B$. (**Right**): individual contributions from rings A and B. The inner ring is fixed at $R_A = 6M$ and $\theta_A = 0°$, while the outer ring in this example has $R_B = 10M$ and $\theta_B = 15°$.

The most important feature of the combined profile is the appearance of a multi-peak structure. Each ring produces its own pair of redshifted and blueshifted peaks. If the two components are sufficiently separated in frequency, the total profile can therefore contain up to four clearly distinguishable peaks. This feature is a direct imprint of the multi-component nature of the emitting source.

To quantify how the outer ring affects the line width, we computed the limiting observed frequencies

$$\nu_{o(\min)} = \nu_{o(\min)}(R_B, \theta_B), \qquad \nu_{o(\max)} = \nu_{o(\max)}(R_B, \theta_B),$$

while keeping the inner ring fixed. The resulting surfaces are shown in Figure 5. They describe how the frequency interval of the outer component changes with its orbital radius and inclination.

The cross-sections in Figure 6 show the same dependence more clearly. Increasing R_B reduces the Keplerian orbital velocity of the outer ring and therefore narrows the corresponding frequency interval. The inclination θ_B changes the projection of the orbital velocity along the line of sight. In the considered configuration this also reduces the separation between the limiting frequencies of the outer-ring contribution. Thus, both the radial position and the mutual inclination of the rings are directly encoded in the width and morphology of the observed spectral line.

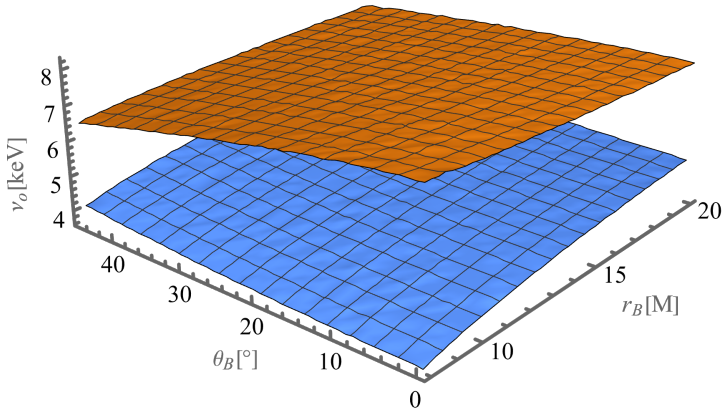

Figure 5. Surface plots of the limiting observed frequencies $\nu_{o(\min)}$ and $\nu_{o(\max)}$ as functions of the radius R_B and inclination θ_B of the outer ring B. The inner ring A is kept fixed at the ISCO, $R_A = 6M$, in the equatorial plane.

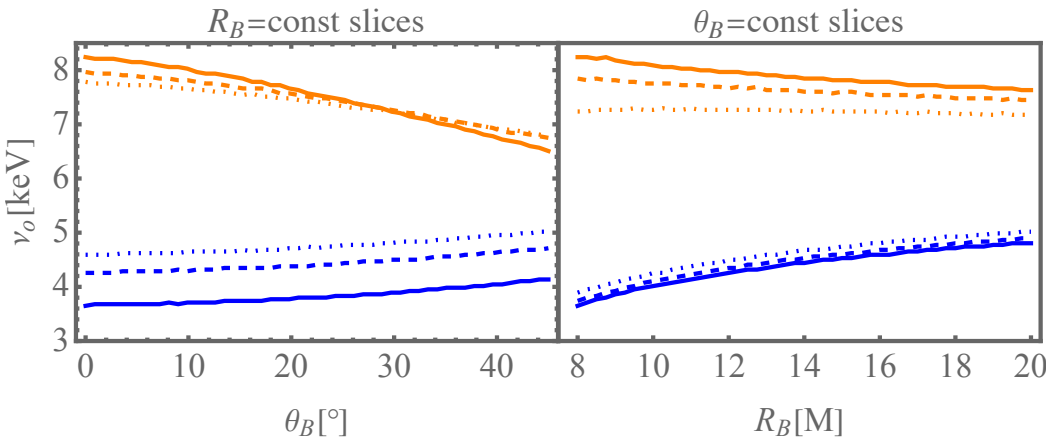

Figure 6. Cross-sections of the surfaces shown in Figure 5. The left panel shows slices at fixed outer-ring radii $R_B = 8M$ solid, $12M$ dashed, and $16M$ dotted. The right panel shows slices at fixed inclinations $\theta_B = 0°$ solid, $15.3°$ dashed, and $29.7°$ dotted.

3.2. Double-Torus System

We now replace the infinitesimally thin rings by finite-thickness toroidal structures. The tori are described by the Polish-doughnut model with constant specific angular momentum, $l_{\rm disk} = {\rm const}$. The parameters of the inner torus A and the outer torus B used in the simulations are listed in Table 2.

Table 2. Parameters of the inner torus A and the outer torus B. For each torus, the values of $l_{\rm disk}$ and W_0 are determined from the conditions $W_0 = W(r_{\rm in}, l_{\rm disk})$ and $W_0 = W(r_{\rm out}, l_{\rm disk})$.

	l_{disk}	W_0	r_{in}	r_{out}
A	3.70328	−0.056239	6.0	8.0
B	3.91918	−0.044616	8.0	12.0

To study the effect of mutual misalignment, we consider the following inclination pattern for the symmetry axes of the two tori:

$$(\theta_{i(A)}, \theta_{i(B)}) = \{(0°, 0°), (0°, 30°), (0°, 45°), (30°, 0°), (45°, 0°)\}\,. \tag{6}$$

For each inclination setup we also vary the relative sense of rotation according to

$$(s_{(A)}, s_{(B)}) = \{(1, 1), (1, -1), (-1, 1)\}\,, \tag{7}$$

where the signs $s_{(A)}$ and $s_{(B)}$ determine the sign of the specific angular momentum of each torus,

$$l_{{\rm disk}(A)} = s_{(A)}|l_{{\rm disk}(A)}|, \qquad l_{{\rm disk}(B)} = s_{(B)}|l_{{\rm disk}(B)}|.$$

Thus, the case $(1, 1)$ corresponds to co-rotation, whereas $(1, -1)$ and $(-1, 1)$ represent counter-rotating configurations.

For each configuration we compute the bolometric flux map on the observer's screen and the corresponding one-dimensional α-profile at fixed $\beta = 1.67$. The horizontal red line in each map indicates the value of β along which the profile is extracted. As a reference, Figure 7 shows the bolometric flux map and α-profile of a single equatorial torus. The double-torus configurations are shown in Figures 8–12.

The reference single-torus image in Figure 7 shows the expected asymmetric flux distribution caused mainly by relativistic Doppler boosting. In the aligned double-torus case, shown in Figure 8, the co-rotating configuration $(s_{(A)}, s_{(B)}) = (1, 1)$ produces a single dominant Doppler-enhanced region in the α-profile. By contrast, the counter-rotating configurations $(1, -1)$ and $(-1, 1)$ produce two dominant flux peaks, because the approaching sides of the two tori appear on opposite sides of the observer's image.

The same distinction between co-rotating and counter-rotating systems is preserved when one of the tori is inclined. However, the mutual misalignment changes the projected velocity field and the visible area of each emitting component. As a result, the relative heights and widths of the Doppler peaks in the α-profiles are modified. The effect is particularly clear when comparing configurations in which the outer torus is tilted, Figures 9 and 10,

with configurations in which the inner torus is tilted, Figures 11 and 12. Therefore, the α-profile provides a compact diagnostic of both the relative rotation sense and the mutual inclination of the two toroidal components.

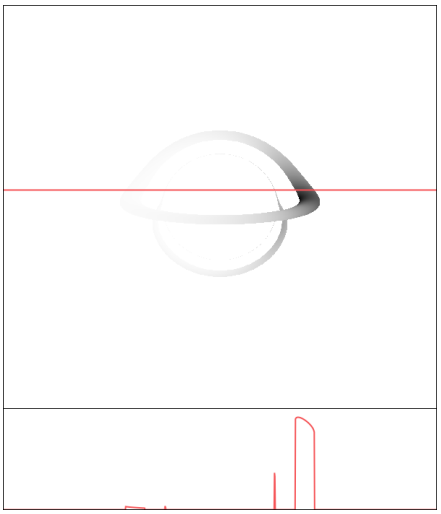

Figure 7. Reference single-torus model. The upper panel shows the bolometric flux map on the observer's screen, and the lower panel shows the corresponding α-profile extracted at $\beta = 1.67$, indicated by the horizontal red line. The torus is equatorial, $\theta_A = 0^\circ$, and rotates with $s_{(A)} = 1$.

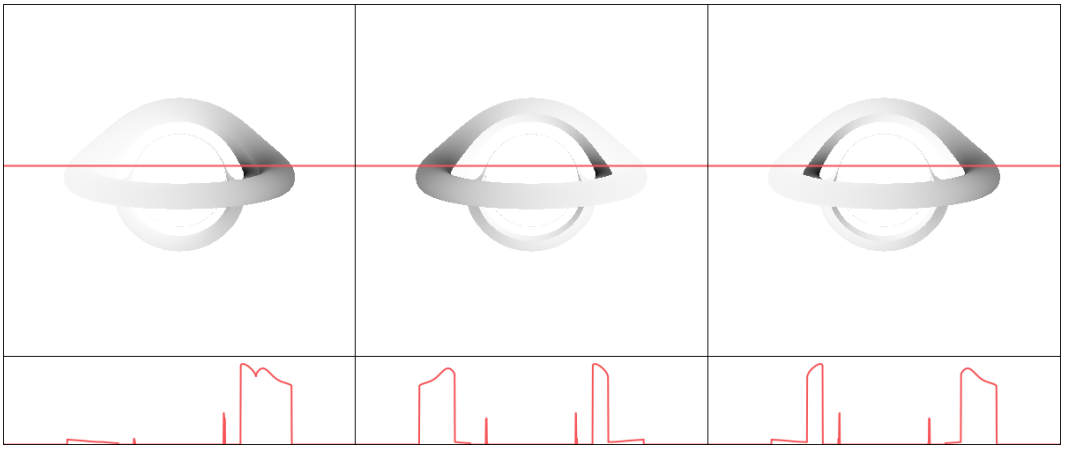

Figure 8. Double-torus bolometric flux maps and corresponding α-profiles for the aligned configuration $(\theta_A, \theta_B) = (0^\circ, 0^\circ)$. The three columns correspond to $(s_{(A)}, s_{(B)}) = (1, 1)$ **left**, $(1, -1)$ **middle**, and $(-1, 1)$ **right**.

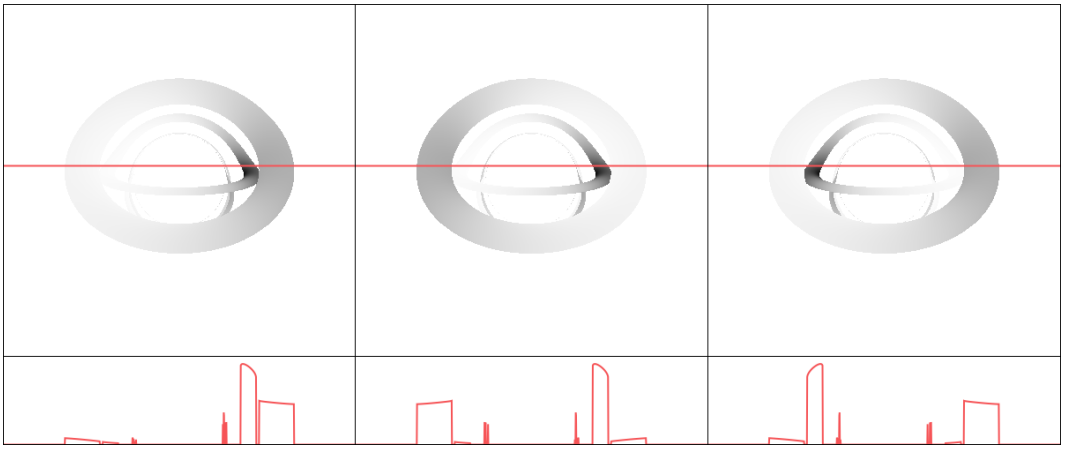

Figure 9. Double-torus bolometric flux maps and corresponding α-profiles for the configuration $(\theta_A, \theta_B) = (0^\circ, 30^\circ)$. The three columns correspond to $(s_{(A)}, s_{(B)}) = (1, 1)$ **left**, $(1, -1)$ **middle**, and $(-1, 1)$ **right**.

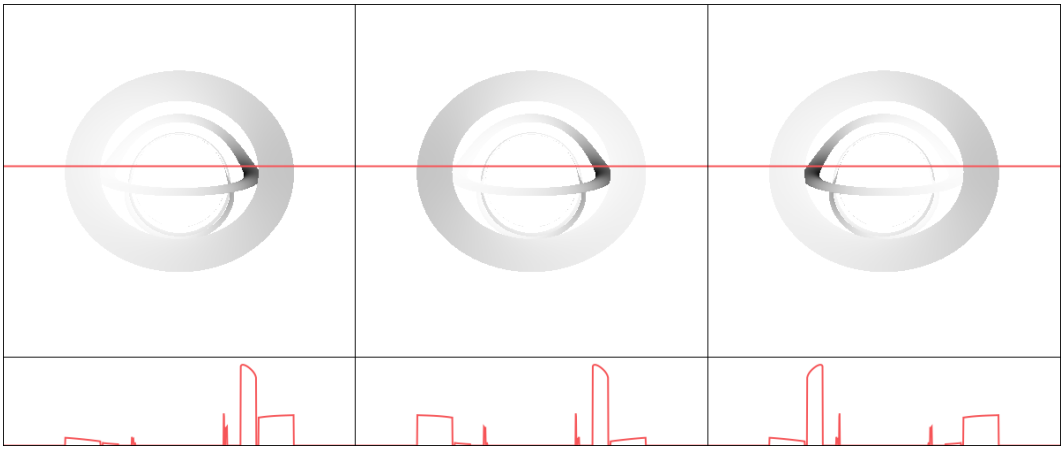

Figure 10. Double-torus bolometric flux maps and corresponding α-profiles for the configuration $(\theta_A, \theta_B) = (0^\circ, 45^\circ)$. The three columns correspond to $(s_{(A)}, s_{(B)}) = (1, 1)$ **left**, $(1, -1)$ **middle**, and $(-1, 1)$ **right**.

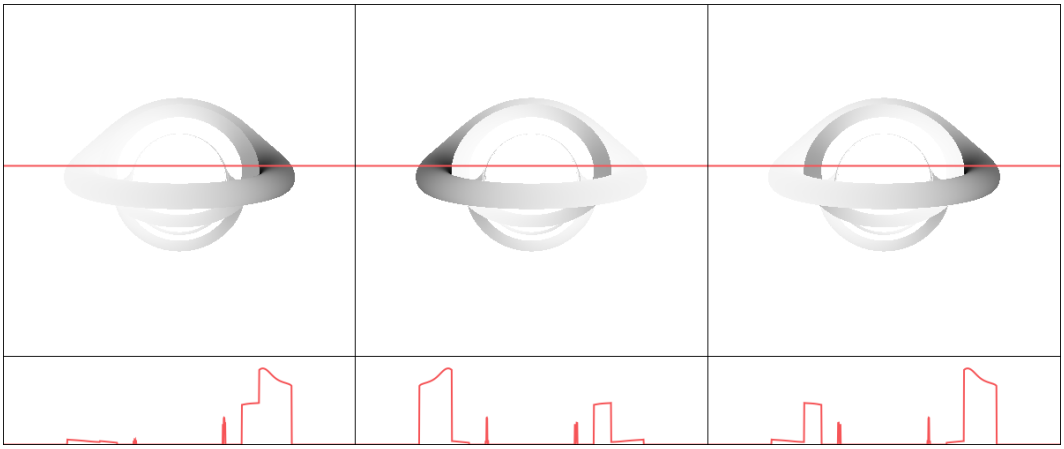

Figure 11. Double-torus bolometric flux maps and corresponding α-profiles for the configuration $(\theta_A, \theta_B) = (30^\circ, 0^\circ)$. The three columns correspond to $(s_{(A)}, s_{(B)}) = (1, 1)$ **left**, $(1, -1)$ **middle**, and $(-1, 1)$ **right**.

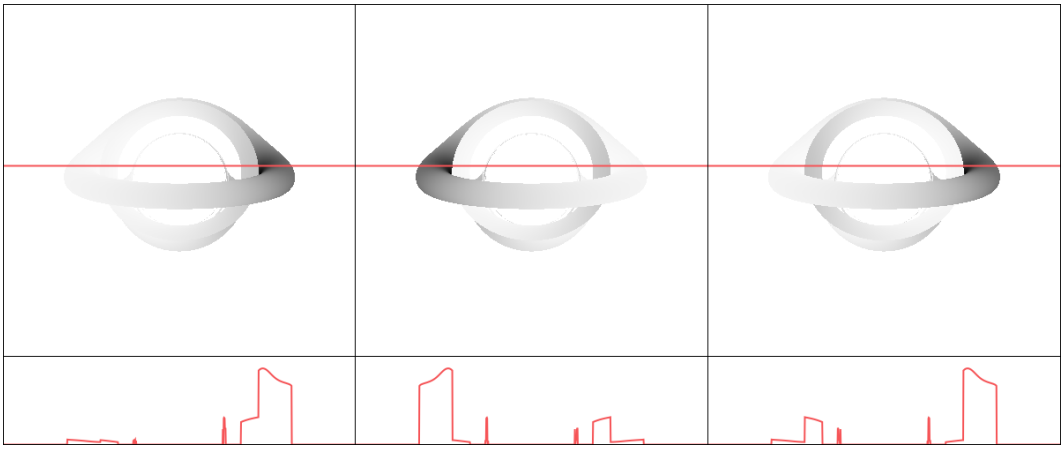

Figure 12. Double-torus bolometric flux maps and corresponding α-profiles for the configuration $(\theta_A, \theta_B) = (45^\circ, 0^\circ)$. The three columns correspond to $(s_{(A)}, s_{(B)}) = (1, 1)$ **left**, $(1, -1)$ **middle**, and $(-1, 1)$ **right**.

4. Discussion

We have studied the ray-traced observational appearance of idealized double-ring and double-torus emitting structures in Schwarzschild spacetime. The main purpose of the model is not to describe a fully self-consistent dynamical equilibrium, but to isolate the effect of a non-coplanar multi-component source on spectral line profiles and bolometric flux distributions. In this sense, the Schwarzschild geometry provides a useful reference case, because the spherical symmetry of the background allows us to change the orientation of the emitting structures

without introducing frame-dragging effects. The differences between the models can therefore be attributed directly to the geometry and motion of the source.

The double-ring model shows that a multi-component source can naturally produce a multi-peak spectral line profile. Each radiating ring gives rise to its own pair of redshifted and blueshifted peaks, and the total profile is their superposition. The appearance of up to four distinguishable peaks therefore does not require a complicated emissivity prescription; it can already arise from two narrow emitting components located at different radii and, in general, in different orbital planes. The radius of the outer ring controls the local Keplerian velocity and hence the width of the corresponding component of the line profile. The inclination of the outer ring changes the projection of the orbital velocity along the line of sight and modifies the separation and relative prominence of the redshifted and blueshifted peaks.

The finite-thickness double-torus model demonstrates that the same basic geometrical effects are also visible in bolometric flux maps. In this case, the observed radiation is affected not only by gravitational redshift and Doppler boosting, but also by the finite size and projected shape of the emitting surfaces. The relative sense of rotation of the two tori has a particularly clear observational imprint. In co-rotating configurations, the Doppler-enhanced regions of the two components tend to appear on the same side of the image and can merge into a single dominant maximum in the α-profile. In counter-rotating configurations, the approaching sides of the two tori are located on opposite sides of the image, producing two dominant peaks in the bolometric-flux profile.

The mutual misalignment of the toroidal axes introduces an additional asymmetry. It changes the visible projected area of each torus and the line-of-sight component of its orbital velocity. As a result, the misalignment is imprinted mainly in the amplitudes, widths, and relative positions of the Doppler-enhanced peaks. The α-profile is therefore a compact diagnostic tool: it preserves information about both the relative rotation sense and the mutual inclination of the emitting components.

The present study should be understood as a simplified radiative experiment. The two tori are prescribed as stationary Polish-doughnut surfaces, and the double structure is treated as an instantaneous radiating configuration. We do not claim that the full non-coplanar double-torus system represents a permanently stable global hydrodynamical equilibrium. Possible dynamical interaction between the tori, mass exchange, turbulence, magnetic fields, self-gravity of the fluid, absorption, scattering, and time-dependent radiative transfer are not included. These effects can be important in realistic accretion flows, but their omission allows us to identify the basic geometrical signatures of non-coplanar double structures in a transparent way.

The results can therefore be used as reference patterns for more sophisticated studies. In particular, the multi-peak line profiles and the one- or two-peak structure of the bolometric α-profiles provide simple signatures against which more realistic GRMHD and radiative-transfer models of tilted, warped, or interacting accretion flows may be compared. A natural continuation of this work would be to extend the model to Kerr spacetime, include time-dependent evolution of interacting tori, and study the role of absorption and emission inside the toroidal matter.

5. Conclusions

We constructed ray-traced models of idealized double-ring and double-torus radiating structures orbiting a Schwarzschild black hole. The two emitting components were allowed to have mutually inclined symmetry axes. The main results can be summarized as follows.

1. A double-ring source produces a spectral line profile that is a superposition of the individual profiles of the two rings. Since each ring generates its own redshifted and blueshifted peak, the combined profile can contain up to four distinguishable peaks.
2. The radius of the outer ring and its inclination with respect to the inner ring are encoded in the width and morphology of the spectral line profile. Increasing the outer-ring radius reduces the orbital velocity and narrows the corresponding frequency interval, while changing the inclination modifies the line-of-sight velocity projection.
3. For finite-thickness double-torus configurations, the relative sense of rotation has a clear imprint on the bolometric flux maps and α-profiles. Co-rotating tori tend to produce one dominant Doppler-enhanced region, whereas counter-rotating configurations can produce two dominant flux peaks on opposite sides of the image.
4. The mutual misalignment of the toroidal axes affects the relative amplitudes, widths, and positions of the Doppler-enhanced peaks. Thus, the α-profile of the bolometric flux provides a simple diagnostic of both the orientation and the rotation sense of the components.
5. Although the model is idealized, it shows that non-coplanar multi-component accretion structures can leave characteristic signatures in spectral line profiles and bolometric-flux distributions. These signatures may be useful for interpreting more realistic simulations of tilted, warped, or interacting accretion flows.

Author Contributions

D.O.: methodology, software, validation, formal analysis, investigation, visualization, writing—original draft preparation, writing—review and editing. J.S.: methodology, software, validation, formal analysis, investigation, visualization, writing—original draft preparation, writing—review and editing. Z.S.: conceptualization, supervision, project administration, funding acquisition, writing—review and editing. All authors have read and agreed to the published version of the manuscript.

Funding

This research was supported by the Research Centre for Theoretical Physics and Astrophysics, Institute of Physics, Silesian University in Opava, and by the Silesian University in Opava under grant No. SGS/24/2024. D.O. also acknowledges support from the grant No. IGS/22/2026.

Institutional Review Board Statement

Not applicable.

Informed Consent Statement

Not applicable.

Data Availability Statement

Not applicable.

Conflicts of Interest

The authors declare no conflict of interest. Given the role as Editorial Board Member, Jan Schee had no involvement in the peer review of this paper and had no access to information regarding its peer-review process. Full responsibility for the editorial process of this paper was delegated to another editor of the journal.

Use of AI and AI-Assisted Technologies

During the preparation of this work, the authors used ChatGPT by OpenAI for language editing and formatting assistance. After using this tool, the authors reviewed and edited the content as needed and take full responsibility for the content of the published article.

Appendix A. Ray Tracing and Coordinate Transformations

In this appendix we summarize the ray-tracing equations and the coordinate transformations used in the construction of the ring and torus images. We use geometrized units $G = c = M = 1$.

Appendix A.1. Null Geodesics in Schwarzschild Spacetime

The Schwarzschild line element is written in the standard form

$$ds^2 = -\left(1 - \frac{2}{r}\right) dt^2 + \left(1 - \frac{2}{r}\right)^{-1} dr^2 + r^2 \left(d\theta^2 + \sin^2\theta \, d\phi^2\right). \tag{A1}$$

For null geodesics, the motion is characterized by the conserved energy $E = -k_t$, the axial angular momentum $L = k_\phi$, and the Carter constant Q. We introduce the impact parameters

$$l = \frac{L}{E}, \qquad q = \frac{Q}{E^2}. \tag{A2}$$

It is useful to use the variables

$$u = \frac{1}{r}, \qquad m = \cos\theta. \tag{A3}$$

The separated radial and latitudinal potentials are

$$U(u; l, q) = 1 - (l^2 + q)u^2 + 2(l^2 + q)u^3, \tag{A4}$$

and

$$M(m; l, q) = q - (l^2 + q)m^2. \tag{A5}$$

For a ring whose orbital plane is inclined with respect to the observer's reference plane, we introduce a coordinate system adapted to the ring. In this system the emitting ring lies in the plane $m_e = 0$. The observer's latitudinal coordinate in the ring-adapted frame is denoted by

$$\bar{m}_o = \cos(\theta_o - \theta_i), \tag{A6}$$

where θ_i is the inclination of the ring plane. Equivalently, if n_i^μ is the unit normal to the i-th ring plane, the inclination can be defined by

$$\cos\theta_i = \tilde{\omega}_\mu^{(3)} n_i^\mu, \tag{A7}$$

where $\tilde{\omega}_\mu^{(3)}$ denotes the spatial tetrad direction normal to the observer's reference equatorial plane.

For a photon emitted from the ring and received by the observer, the radial and latitudinal parts of the null geodesic are related by Carter's integral equation

$$\int_{u_o}^{u_e} \frac{\mathrm{d}u}{\sqrt{U(u;l,q)}} - m_{\mathrm{sgn}} \int_{\bar{m}_o}^{0} \frac{\mathrm{d}m}{\sqrt{M(m;l,q)}} = 0. \tag{A8}$$

Here u_o and u_e are the inverse radial coordinates of the observer and emitter, respectively. The factor $m_{\mathrm{sgn}} = \pm 1$ specifies the initial direction of the latitudinal motion. Equation (A8) is the form used to determine the impact parameters of photon trajectories connecting the observer with a point on the emitting ring when no additional turning-point contribution is written explicitly.

More generally, if the photon trajectory contains radial or latitudinal turning points, the integrals in Equation (A8) are understood as sums over the corresponding monotonic parts of the motion. We denote this generalized form as

$$\mathcal{I}_u(u_o, u_e; n_u) - m_{\mathrm{sgn}} \mathcal{I}_m(\bar{m}_o, 0; n_m) = 0. \tag{A9}$$

The integers n_u and n_m count the number of radial and latitudinal turning points along the photon trajectory. The turning points are determined by the roots of

$$U(u;l,q) = 0, \qquad M(m;l,q) = 0. \tag{A10}$$

In the present work we include the primary image contributions specified by

$$(n_u, n_m) = \{(0,0), (0,1), (1,1)\}. \tag{A11}$$

The contribution $(0,0)$ corresponds to a direct trajectory without turning points, $(0,1)$ includes one latitudinal turning point, and $(1,1)$ includes one radial and one latitudinal turning point. In the numerical implementation the relevant turning-point contributions are added to the radial and latitudinal integrals in Equation (A9).

The observer's screen coordinates (α, β) are related to the impact parameters by

$$l = \alpha\sqrt{1 - m_o^2}, \qquad q = \beta^2 + m_o^2\alpha^2, \tag{A12}$$

where $m_o = \cos\theta_o$ is the observer's latitudinal coordinate in the global Schwarzschild frame. Each point on the observer's image plane therefore defines one null geodesic through the parameters l and q. For the inclined-ring calculation, the same geodesic is evaluated in the ring-adapted frame, where the observer coordinate entering Equation (A8) is $\bar{m}_o$.

Appendix A.2. Spectral Line Profile of a Ring

For the ring model, the observed specific flux is computed by integrating over the redshift factor $g = \nu_o/\nu_e$. For a narrow emitting ring at radius r_e, we use

$$F(\nu_o; r_e) = \Delta r_e \int_{g_{\min}}^{g_{\max}} g^3 I_e(\nu_o/g; r_e) \left| \frac{\partial(\alpha,\beta)}{\partial(r_e, g)} \right| dg. \tag{A13}$$

The factor g^3 follows from the invariance of I_ν/ν^3 along a null geodesic. The Jacobian

$$\left| \frac{\partial(\alpha,\beta)}{\partial(r_e, g)} \right| \tag{A14}$$

is evaluated numerically from the ray-tracing map $(\alpha, \beta) \mapsto (r_e, g)$. Equivalently,

$$\left|\frac{\partial(\alpha,\beta)}{\partial(r_e,g)}\right| = \left|\frac{\partial(r_e,g)}{\partial(\alpha,\beta)}\right|^{-1}. \tag{A15}$$

Appendix A.3. Rotated Coordinate Frame for an Inclined Torus

For a torus whose symmetry axis is inclined with respect to the original equatorial axis, we introduce a source-adapted coordinate system (r', θ', ϕ'). The primed frame is obtained by a rotation of the source-adapted spatial triad about the original y-axis by the angle θ_i. Equivalently, the new symmetry axis lies in the original $x - z$ plane, with x-axis directed towards the observer, and has the direction

$$\mathbf{e}_{z'} = \sin\theta_i\, \mathbf{e}_x + \cos\theta_i\, \mathbf{e}_z. \tag{A16}$$

The remaining basis vectors may be chosen as

$$\mathbf{e}_{x'} = \cos\theta_i\, \mathbf{e}_x - \sin\theta_i\, \mathbf{e}_z, \qquad \mathbf{e}_{y'} = \mathbf{e}_y. \tag{A17}$$

With this convention, the transformation between the original spherical coordinates (r, θ, ϕ) and the rotated coordinates (r', θ', ϕ') is

$$r' = r, \tag{A18}$$

$$\cos\theta' = \sin\theta\cos\phi\sin\theta_i + \cos\theta\cos\theta_i, \tag{A19}$$

and

$$\tan\phi' = \frac{\sin\theta\sin\phi}{\sin\theta\cos\phi\cos\theta_i - \cos\theta\sin\theta_i}. \tag{A20}$$

In numerical calculations it is preferable to use the two-argument arctangent function

$$\phi' = \mathrm{atan2}\left(\sin\theta\sin\phi,\ \sin\theta\cos\phi\cos\theta_i - \cos\theta\sin\theta_i\right), \tag{A21}$$

which fixes the correct quadrant of ϕ'. Here, $\mathrm{atan2}(Y, X)$ denotes the two-argument arctangent. It returns the angle $\phi' \in (-\pi, \pi]$ such that

$$\cos\phi' = \frac{X}{\sqrt{X^2+Y^2}}, \qquad \sin\phi' = \frac{Y}{\sqrt{X^2+Y^2}},$$

with the quadrant of ϕ' determined by the signs of X and Y.

The components of a photon wave vector

$$k^\mu = (k^t, k^r, k^\theta, k^\phi) \tag{A22}$$

transform to the primed frame according to

$$k^{\mu'} = \frac{\partial x^{\mu'}}{\partial x^\nu} k^\nu. \tag{A23}$$

The non-zero elements required in the present calculation are

$$\frac{\partial t'}{\partial t} = 1, \qquad \frac{\partial r'}{\partial r} = 1, \tag{A24}$$

$$\frac{\partial\theta'}{\partial\theta} = -\frac{\cos\theta\cos\phi\sin\theta_i - \sin\theta\cos\theta_i}{\sqrt{1-\left(\sin\theta\cos\phi\sin\theta_i + \cos\theta\cos\theta_i\right)^2}}, \tag{A25}$$

$$\frac{\partial\theta'}{\partial\phi} = \frac{\sin\theta\sin\phi\sin\theta_i}{\sqrt{1-\left(\sin\theta\cos\phi\sin\theta_i + \cos\theta\cos\theta_i\right)^2}}. \tag{A26}$$

It is convenient to define

$$X = \sin\theta\cos\phi\cos\theta_i - \cos\theta\sin\theta_i, \qquad Y = \sin\theta\sin\phi, \tag{A27}$$

so that

$$\phi' = \mathrm{atan2}(Y, X), \qquad X^2 + Y^2 = \sin^2\theta'. \tag{A28}$$

Then

$$\frac{\partial\phi'}{\partial\theta} = -\frac{\sin\phi\sin\theta_i}{X^2+Y^2}, \tag{A29}$$

and

$$\frac{\partial\phi'}{\partial\phi} = \frac{\sin^2\theta\cos\theta_i - \sin\theta\cos\theta\cos\phi\sin\theta_i}{X^2+Y^2}. \tag{A30}$$

For $\theta_i = 0$, the primed and unprimed frames coincide:

$$\theta' = \theta, \qquad \phi' = \phi.$$

Appendix A.4. Geodesic Integration for the Torus Images

For the construction of torus images we integrate the geodesic equations in terms of $u = 1/r$ and $m = \cos\theta$. The relevant geodesic equations for null vector k^μ in the form [26] are

$$\frac{dk^u}{d\lambda} = 2u^3\left(U + \frac{u}{4}\frac{dU}{du}\right), \tag{A31}$$

$$\frac{dk^m}{d\lambda} = \frac{2}{u}k^u k^m + \frac{1}{2}u^4\frac{dM}{dm}, \tag{A32}$$

$$\frac{d\phi}{d\lambda} = \frac{u^2 l}{1-m^2}. \tag{A33}$$

Here $U = U(u; l, q)$ and $M = M(m; l, q)$ are the potentials defined above. For a given observer position (u_o, m_o) and screen coordinates (α, β), the initial values are

$$k^u_o = u_o^2\sqrt{1 - u_o^2(l^2+q)(1-2u_o)}, \tag{A34}$$

$$k^m_o = u_o^2\sqrt{q - m_o^2(l^2+q)}, \tag{A35}$$

$$\phi_o = 0. \tag{A36}$$

The signs of k^u_o and k^m_o are chosen according to the required direction of backward ray tracing from the observer to the emitting surface.

Appendix A.5. Intersection with a Torus and Frequency Shift

The torus surface is defined by a constant value of the effective potential,

$$W(r, \theta') = W_0. \tag{A37}$$

During the ray-tracing procedure we search for intersections of a null geodesic with the surfaces of both tori. If a photon intersects both emitting surfaces, the contribution with the smaller value of the affine parameter λ is used, corresponding to the first surface reached by the photon when traced backward from the observer.

The frequency shift is defined as

$$g = \frac{\nu_o}{\nu_e} = \frac{(k_\mu u^\mu)_o}{(k_\mu u^\mu)_e}. \tag{A38}$$

For a static observer at infinity and a circularly rotating emitter in the primed torus frame, this gives

$$g = \frac{\sqrt{1 - \frac{2}{r} - r^2\sin^2\theta'\,\Omega^2}}{1 - l'\Omega}. \tag{A39}$$

The angular velocity of the perfect-fluid torus is

$$\Omega = \frac{\left(1 - \frac{2}{r}\right) l_{\mathrm{disk}}}{r^2\sin^2\theta'}. \tag{A40}$$

The quantity l' is the photon impact parameter with respect to the rotated azimuthal coordinate,

$$l' = -\frac{k_{\phi'}}{k_t}. \tag{A41}$$

In the numerical implementation it is evaluated from the transformed photon momentum $k^{\mu'}$, rather than from the unprimed value of l alone. Explicitly,

$$k^{\phi'} = \frac{\partial \phi'}{\partial \theta} k^{\theta} + \frac{\partial \phi'}{\partial \phi} k^{\phi}, \tag{A42}$$

and hence

$$l' = \frac{r^2 \sin^2 \theta' \, k^{\phi'}}{\left(1 - \frac{2}{r}\right) k^t}. \tag{A43}$$

This definition is invariantly equivalent to Equation (A41) and is the safest way to evaluate the redshift for an inclined torus.

Appendix A.6. Bolometric Flux and Line Profile

Using Liouville's theorem, the bolometric intensity transforms as $I_o = g^4 I_e$. Therefore, the bolometric flux map on the observer's screen is computed as

$$F_o(\alpha_i, \beta_j) = g^4_{(ij)} I_{e(ij)}. \tag{A44}$$

For spectral line calculations we use the transformation of the specific intensity, $I_{\nu_o} = g^3 I_{\nu_e}$, and write

$$F_{\nu_o} = \sum_{i=1}^{N} g^3_{(i)} I_{\nu_e(i)}. \tag{A45}$$

The local emissivity is modeled as a Gaussian line,

$$I_{\nu_e(i)} = \epsilon_0 \exp\left[-\frac{1}{\sigma^2} \left(\frac{\nu_o}{g_{(i)}} - \nu_0 \right)^2 \right]. \tag{A46}$$

Equations (A44)–(A46) are used to construct both the bolometric flux maps and the spectral line profiles of the double-torus configurations.

References

1. Akiyama, K.; Alberdi, A.; Alef, W.; et al. First M87 Event Horizon Telescope Results. I. The Shadow of the Supermassive Black Hole. *Astrophys. J. Lett.* **2019**, *875*, L1. https://doi.org/10.3847/2041-8213/ab0ec7.
2. Akiyama, K.; Alberdi, A.; Alef, W.; et al. First Sagittarius A* Event Horizon Telescope Results. I. The Shadow of the Supermassive Black Hole in the Center of the Milky Way. *Astrophys. J. Lett.* **2022**, *930*, L12. https://doi.org/10.3847/2041-8213/ac6674.
3. Akiyama, K.; Alberdi, A.; Alef, W.; et al. First M87 Event Horizon Telescope Results. V. Physical Origin of the Asymmetric Ring. *Astrophys. J. Lett.* **2019**, *875*, L5. https://doi.org/10.3847/2041-8213/ab0f43.
4. Akiyama, K.; Alberdi, A.; Alef, W.; et al. First Sagittarius A* Event Horizon Telescope Results. V. Testing Astrophysical Models of the Galactic Center Black Hole. *Astrophys. J. Lett.* **2022**, *930*, L16. https://doi.org/10.3847/2041-8213/ac6672.
5. Mościbrodzka, M.; Gammie, C.F. IPOLE: semi-analytic scheme for relativistic polarized radiative transport. *Mon. Not. R. Astron. Soc.* **2018**, *475*, 43–54. https://doi.org/10.1093/mnras/stx3162.
6. Shakura, N.I.; Sunyaev, R.A. Black holes in binary systems. Observational appearance. *Astron. Astrophys.* **1973**, *24*, 337–355.
7. Novikov, I.D.; Thorne, K.S. Astrophysics of Black Holes. In *Black Holes*; DeWitt, C., DeWitt, B.S., Eds.; Gordon and Breach: New York, NY, USA, 1973; pp. 343–450.
8. Pringle, J.E.; Rees, M.J. Accretion Disc Models for Compact X-Ray Sources. *Astron. Astrophys.* **1972**, *21*, 1–9.
9. Cunningham, C.T. The effects of redshifts and focusing on the spectrum of an accretion disk around a Kerr black hole. *Astrophys. J.* **1975**, *202*, 788–802.
10. Fabian, A.C.; Rees, M.J.; Stella, L.; et al. X-ray fluorescence from the inner disc in Cygnus X-1. *Mon. Not. R. Astron. Soc.* **1989**, *238*, 729–736. https://doi.org/10.1093/mnras/238.3.729.
11. Laor, A. Line profiles from a disk around a rotating black hole. *Astrophys. J.* **1991**, *376*, 90–94. https://doi.org/10.1086/170257.

12. Karas, V.; Sochora, V. Extremal energy shifts of radiation from a ring near a rotating black hole. *Astrophys. J.* **2010**, *725*, 1507–1515. https://doi.org/10.1088/0004-637X/725/2/1507.
13. Sochora, V.; Karas, V.; Svoboda, J.; et al. Black hole accretion rings revealed by future X-ray spectroscopy. *Mon. Not. R. Astron. Soc.* **2011**, *418*, 276–283. https://doi.org/10.1111/j.1365-2966.2011.19483.x.
14. Fishbone, L.G.; Moncrief, V. Relativistic fluid disks in orbit around Kerr black holes. *Astrophys. J.* **1976**, *207*, 962–976.
15. Abramowicz, M.A.; Jaroszyński, M.; Sikora, M. Relativistic, accreting disks. *Astron. Astrophys.* **1978**, *63*, 221–224.
16. Kozłowski, M.; Jaroszyński, M.; Abramowicz, M.A. The analytic theory of fluid disks orbiting the Kerr black hole. *Astron. Astrophys.* **1978**, *63*, 209–220.
17. Wu, S.M.; Wang, T.G. Iron line profiles and self-shadowing from relativistic thick accretion discs. *Mon. Not. R. Astron. Soc.* **2007**, *378*, 841–851. https://doi.org/10.1111/j.1365-2966.2007.11855.x.
18. Pugliese, D.; Stuchlík, Z. Ringed Accretion Disks: Evolution of Double Toroidal Configurations. *Astrophys. J. Suppl. Ser.* **2017**, *229*, 40. https://doi.org/10.3847/1538-4365/aa68e6.
19. Pugliese, D.; Stuchlík, Z. Ringed Accretion Disks: Equilibrium Configurations. *The Astrophysical Journal Supplement Series* **2015**, *221*, 25. https://doi.org/10.1088/0067-0049/221/2/25.
20. Bardiev, D.; Kološ, M.; Pugliese, D.; et al. GRMHD Evolution of Interacting Double Accretion Tori Orbiting a Central Black Hole. *Astrophys. J.* **2022**, *941*, 173. https://doi.org/10.3847/1538-4357/aca0a3.
21. Dexter, J.; Fragile, P.C. Observational Signatures of Tilted Black Hole Accretion Disks from Simulations. *Astrophys. J.* **2011**, *730*, 36. https://doi.org/10.1088/0004-637X/730/1/36.
22. Nixon, C.; King, A.; Price, D.; et al. Tearing up the disk: how black holes accrete. *Astrophys. J. Lett.* **2012**, *757*, L24. https://doi.org/10.1088/2041-8205/757/2/L24.
23. Nealon, R.; Price, D.J.; Nixon, C.J. On the Bardeen–Petterson effect in black hole accretion discs. *Mon. Not. R. Astron. Soc.* **2015**, *448*, 1526–1540. https://doi.org/10.1093/mnras/stv014.
24. Pugliese, D.; Stuchlík, Z. Limiting effects in clusters of misaligned toroids orbiting static SMBHs. *Mon. Not. R. Astron. Soc.* **2020**, *493*, 4229–4255. https://doi.org/10.1093/mnras/staa503.
25. Pugliese, D.; Stuchlík, Z. Embedded BHs and multipole globules: clustered misaligned thick accretion disks around static SMBHs. *Class. Quantum Gravity* **2020**, *37*, 195025. https://doi.org/10.1088/1361-6382/ab995b.
26. Schee, J.; Stuchlík, Z. Appearance of Keplerian discs orbiting on both sides of reflection-symmetric wormholes. *J. Cosmol. Astropart. Phys.* **2022**, *2022*, 054. https://doi.org/10.1088/1475-7516/2022/01/054.